

Impact of stellar winds on the pair-instability supernova rate

Filippo Simonato^{1,2,3*}, Stefano Torniamenti^{4,5**}, Michela Mapelli^{***1,2,5,6,7}, Giuliano Iorio⁸, Lumen Boco⁵,
Franca De Domenico-Langer⁵, and Cecilia Sgalletta^{9,10,11}

¹Physics and Astronomy Department Galileo Galilei, University of Padova, Vicolo dell'Osservatorio 3, I-35122, Padova, Italy

²Gran Sasso Science Institute (GSSI), Viale Francesco Crispi 7, 67100 L'Aquila, Italy

³INFN, Laboratori Nazionali del Gran Sasso, 67100 Assergi, Italy

⁴Max-Planck-Institut für Astronomie, Königstuhl 17, 69117, Heidelberg, Germany

⁵Universität Heidelberg, Zentrum für Astronomie (ZAH), Institut für Theoretische Astrophysik, Albert-Ueberle-Str. 2, 69120, Heidelberg, Germany

⁶ Universität Heidelberg, Interdisziplinäres Zentrum für Wissenschaftliches Rechnen, Heidelberg, Germany

⁷INFN, Sezione di Padova, Via Marzolo 8, I-35131 Padova, Italy

⁸Departament de Física Quàntica i Astrofísica, Institut de Ciències del Cosmos, Universitat de Barcelona, Martí i Franquès 1, E-08028 Barcelona, Spain

⁹SISSA, via Bonomea 365, I-34136 Trieste, Italy

¹⁰National Institute for Nuclear Physics – INFN, Sezione di Trieste, I-34127 Trieste, Italy

¹¹Istituto Nazionale di Astrofisica – Osservatorio Astronomico di Roma, Via Frascati 33, I-00040, Monteporzio Catone, Italy

Received XXXX; accepted YYYY

ABSTRACT

Very massive stars (VMSs, $M_{\star} \geq 100 M_{\odot}$) play a crucial role in several astrophysical processes. At low metallicity, they might collapse directly into black holes, or end their lives as pair-instability supernovae. Recent observational results set an upper limit of $0.7 \text{ yr}^{-1} \text{ Gpc}^{-3}$ on the rate density of pair-instability supernovae in the nearby Universe. However, most theoretical models predict rates exceeding this limit. Here, we compute new VMS tracks with the MESA code, and use them to analyze the evolution of the (pulsational) pair-instability supernova rate density across cosmic time. We show that stellar wind models accounting for the transition between optically thin and thick winds yield a pair-instability supernova rate $\mathcal{R}_{\text{PISN}} \sim 0.1 \text{ Gpc}^{-3} \text{ yr}^{-1}$ at redshift $z \sim 0$, about two orders of magnitude lower than our previous models. We find that the main contribution to the pair-instability supernova rate comes from stars with metallicity $Z \sim 0.001 - 0.002$. Stars with higher metallicities cannot enter the pair-instability supernova regime, even if their zero-age main sequence mass is up to $500 M_{\odot}$. The main reason is that VMSs enter the regime for optically thick winds during the main sequence at metallicity as low as $Z \sim 4 \times 10^{-4}$. This enhances the mass loss rate, quenching the growth of the He core and thus preventing the onset of pair-instability in later evolutionary stages. This result highlights the critical role of mass loss in shaping the final fate of very massive stars and the rate of pair-instability supernovae.

Key words. Stars: mass-loss – Stars: massive – Stars: black holes

1. Introduction

Very massive stars (VMSs), with an initial mass $> 100 M_{\odot}$, represent a challenge to our understanding of stellar evolution due to their extreme physical properties. Several studies have explored their evolutionary paths (Belkus et al. 2007; Yungelson et al. 2008; Gräfenor et al. 2011; Brott et al. 2011; Georgy et al. 2013; Yusof et al. 2013; Hirschi 2015; Limongi & Chieffi 2018) and their observational properties in the local Universe (Crowther et al. 2010; Bestenlehner et al. 2014).

As VMSs evolve, they lose mass via stellar winds, including nitrogen and other products of hot hydrogen burning. Hence, they might be one of the main sources of the N enhancement observed in some compact high-redshift galaxies (Vink 2023; Cameron et al. 2023; Charbonnel et al. 2023; Gieles et al. 2025). Several works show that, if they directly collapse onto a black hole, VMSs can form intermediate-mass black holes (IMBHs, with mass $> 10^2 M_{\odot}$, Ebisuzaki et al. 2001; Heger & Woosley

2002; Portegies Zwart & McMillan 2002; Portegies Zwart et al. 2004, 2005; Giersz et al. 2015; Mapelli 2016; Spera & Mapelli 2017; Costa et al. 2023).

If VMSs do not undergo direct collapse at the end of their life but instead explode as supernovae, they release enormous amounts of material into the interstellar medium (Ohkubo et al. 2006; Yokoyama & Tominaga 2012; Kojima et al. 2021; Goswami et al. 2022; Vink 2023). Specifically, one of the possible final fates of VMSs is a pair-instability supernova (PISN) (Heger & Woosley 2002; Woosley 2017; Spera & Mapelli 2017). PISNe occur when the efficient formation of electron-positron pairs softens the equation of state of the carbon-oxygen core (Barkat et al. 1967; Fraley 1968; Bond et al. 1984; Heger & Woosley 2002). The resulting contraction of the core triggers explosive burning of oxygen and silicon. As a consequence, the star may undergo a single, powerful explosion that leaves no compact remnant (PISN), or it may experience multiple pulsations before ultimately collapsing into a black hole (pulsational pair-instability supernova, PPISN; Woosley et al. 2002; Chen et al. 2014; Yoshida et al. 2016; Woosley 2017). Since the onset of the instability depends on the central density and temperature,

* e-mail: filippo.simonato@gssi.it

** e-mail: storniamenti@mpia.de

*** e-mail: mapelli@uni-heidelberg.de

the final mass of the helium core ($M_{\text{He},f}$) is a good proxy to infer whether a star enters the pair-instability regime or not: according to Woosley (2017), if $32 M_{\odot} \leq M_{\text{He},f} < 64 M_{\odot}$, it undergoes a PPISN; if $64 M_{\odot} \leq M_{\text{He},f} < 135 M_{\odot}$, it explodes in a PISN; otherwise, if $M_{\text{He},f} > 135 M_{\odot}$, it collapses directly onto an IMBH.

PISNe and PPISNe may have a deep impact on the mass function of black holes, as they are expected to open a gap between ≈ 60 and $\approx 120 M_{\odot}$ (Woosley 2017; Spera & Mapelli 2017). Our knowledge of these boundaries is however affected by multiple sources of uncertainties, concerning nuclear reaction rates, stellar rotation, convection, and the energetics of failed supernovae (e.g., Leung et al. 2019; Farmer et al. 2019, 2020; Mapelli et al. 2020; Marchant & Moriya 2020; Renzo et al. 2020; Song et al. 2020; Tanikawa et al. 2021; Farrell et al. 2021; Vink et al. 2021; Woosley & Heger 2021; Farag et al. 2022; Hendriks et al. 2023; Winch et al. 2025).

As for observations, we still lack an uncontroversial detection of a (P)PISN, even if several studies reported possible candidates (Woosley et al. 2007; Gal-Yam et al. 2009; Quimby et al. 2011; Cooke et al. 2012; Kozyreva & Blinnikov 2015; Kozyreva et al. 2018; Mazzali et al. 2019). The supernova SN2018ibb is possibly the strongest PISN candidate reported to date (Schulze et al. 2024). The same authors estimated that the rate density of PISNe $\mathcal{R}_{\text{PISN}}$ should lie between $0.009 \text{ yr}^{-1} \text{ Gpc}^{-3}$ and $0.7 \text{ yr}^{-1} \text{ Gpc}^{-3}$ at 2σ confidence, based on the spectroscopically complete ZTF Bright Transient survey of superluminous supernovae (Fremling et al. 2020; Perley et al. 2020).

Theoretical models estimate the PISN rate to be between 10^{-5} and 10^{-2} times the core-collapse supernova rate (Langer et al. 2007; Briel et al. 2022), but such estimates are affected by uncertainties about the initial mass function and metallicity of the progenitors (Langer et al. 2007), the cosmic star formation history (Briel et al. 2022; Gabrielli et al. 2024), models of stellar evolution (Takahashi 2018; du Buisson et al. 2020; Farmer et al. 2020; Tanikawa et al. 2023; Gabrielli et al. 2024), and whether the progenitor evolves as an isolated star or in a binary system (Briel et al. 2022; Tanikawa et al. 2023).

Briel et al. (2022, hereafter B22) investigated how star-forming environments influence electromagnetic and gravitational-wave transients by employing empirical models (Madau & Dickinson 2014) and cosmological simulations (EAGLE, Schaye et al. 2015; Crain et al. 2015; ILLUSTRISTNG, Springel et al. 2005; Nelson et al. 2018; Pillepich et al. 2018; Naiman et al. 2018; Marinacci et al. 2018; MILLENNIUM, Springel et al. 2005). Among their models, the only one consistent with the upper limit found by Schulze et al. (2024) is based on the EAGLE simulation (Schaye et al. 2015), combined with the B-PASS population synthesis models (Eldridge et al. 2017). In a follow-up study, Briel et al. (2024) focus on the ILLUSTRISTNG simulation and obtain an expected PISN rate density $\mathcal{R}_{\text{PISN}} = 2 - 29 \text{ Gpc}^{-3} \text{ yr}^{-1}$ at redshift $z = 0$, by quantifying the uncertainties from their binary evolutionary models.

Tanikawa et al. (2023, hereafter T23) explored the influence of the $^{12}\text{C}(\alpha,\gamma)^{16}\text{O}$ reaction rate on the PISN rate in models of binary populations. By adopting the standard reaction rate and assuming a maximum zero-age main-sequence (ZAMS) mass of $300 M_{\odot}$, they found $\mathcal{R}_{\text{PISN}} \geq 1 \text{ yr}^{-1} \text{ Gpc}^{-3}$. In contrast, using a 3σ lower reaction rate, they found $\mathcal{R}_{\text{PISN}} \ll 1 \text{ yr}^{-1} \text{ Gpc}^{-3}$. The critical role of the $^{12}\text{C}(\alpha,\gamma)^{16}\text{O}$ reaction rate has been largely debated in the context of the pair-instability mass gap of black holes, with lower rates leading to higher black hole masses below the gap (e.g., Farmer et al. 2019, 2020; Costa et al. 2021; Woosley & Heger 2021).

Gabrielli et al. (2024, hereafter G24) explored various criteria for the onset of pair instability, including the impact of the metallicity threshold for PISNe, the maximum ZAMS mass, and the dispersion in the metallicity distribution of the host galaxies. They found that all these quantities affect the PISN rate, resulting in a seven orders of magnitude variation up to $\mathcal{R}_{\text{PISN}} \sim 2000 \text{ yr}^{-1} \text{ Gpc}^{-3}$. According to their analysis (Fig. 8 from Gabrielli et al. 2024), only models with a metallicity threshold for the onset of pair instability $Z \leq 1.5 \times 10^{-3}$, a maximum ZAMS star mass $M_{\text{ZAMS}} \leq 150 M_{\odot}$, and a narrow metallicity spread yield rates $\mathcal{R}_{\text{PISN}} < 1 \text{ Gpc}^{-3} \text{ yr}^{-1}$. This result confirms that the PISN rate is very sensitive to the assumed metallicity threshold for the onset of PISNe. Moreover, assuming a narrow metallicity dispersion suppresses pockets of low-metallicity star formation in the nearby Universe (Boco et al. 2019; Santoliquido et al. 2022).

In summary, most theoretical estimates of the PISN rate density exceed the upper limit reported by Schulze et al. (2024). The only models that yield PISN rates below this upper limit assume low values for the $^{12}\text{C}(\alpha,\gamma)^{16}\text{O}$ reaction rate, enforce a low metallicity threshold for the onset of PISNe, suppress the low-metallicity tails of star formation in the nearby Universe, and/or put a cap on the maximum ZAMS mass. The upper limit to the maximum ZAMS mass is particularly critical, because we have observed stars with $M_{\text{ZAMS}} > 150 M_{\odot}$ even in the local Universe (Crowther et al. 2010; Bestenlehner et al. 2014, 2020).

Here, we explore an alternative scenario inspired by recent models of optically thick winds for VMSs (Sabhahit et al. 2023, hereafter S23). This scenario does not require to fine tune the $^{12}\text{C}(\alpha,\gamma)^{16}\text{O}$ reaction rate, works for a realistic evolution of the metallicity spread in galaxies, and does not require to cap the maximum star mass, while it naturally leads to a low metallicity threshold Z_{th} for the activation of PISNe ($Z_{\text{th}} \sim Z_{\odot}/10$, S23).

Recent models of mass loss by stellar winds (Vink et al. 2011; Sabhahit et al. 2022, 2023) indicate that VMSs develop optically thick winds already on the main sequence, becoming WNh stars (Bestenlehner et al. 2020). The transition between optically thin winds of O-type stars and optically thick ones is a function of the electron-scattering Eddington ratio Γ_{Edd} . At the metallicity of the Large Magellanic Cloud and even the Small Magellanic Cloud, this model strips the H-rich envelope of VMSs completely, without the need for mass loss through binary interaction. Here, we investigate the impact of such new stellar wind models (S23) on the expected PISN and PPISN rate density. We show that a larger mass-loss rate for VMSs at intermediate metallicity (down to $Z \sim 0.002$, S23) seems to be the key to predicting PISN rates in agreement with the observational constraints.

This paper is organized as follows. We briefly describe the physics and the prescription adopted to the (P)PISN rate density in Sec. 2. In Sec. 3, we show the rate densities obtained with the two different stellar models. We discuss the impact of an enhanced mass-loss rate in Sec. 4. Finally, our results are summarized in Sec. 5.

2. Method

We use the stellar evolution code MESA (version r12115; Paxton et al. 2011, 2013, 2015, 2018, 2019) to model massive stars and VMSs and produce stellar tables for the population synthesis code SEVN (Spera & Mapelli 2017; Spera et al. 2019; Mapelli et al. 2020; Iorio et al. 2023). Then, we combine our population synthesis models with a metal-dependent star formation rate density history by means of the semi-analytic code COSMORATE

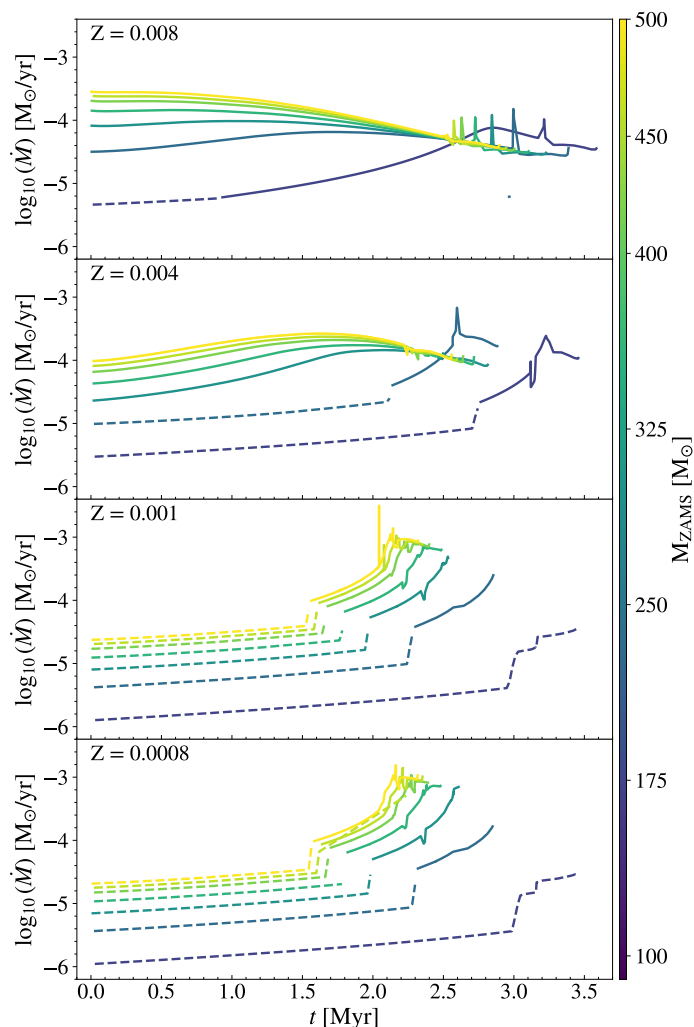


Fig. 1: Mass-loss rate of our MESA models as a function of time, from the ZAMS until the end of core He burning. The models adopt the winds by Sabhahit et al. (2023). From top to bottom: $Z = 0.008, 0.004, 0.001,$ and 0.0008 . The solid lines correspond to the evolutionary phase in which the stellar models are in the optically thick regime ($\Gamma_{\text{Edd}} > \Gamma_{\text{Edd,tr}}$), while the dashed lines mark the optically thin regime.

(Santoliquido et al. 2021, 2022). Here below, we describe our methodology in detail.

2.1. Stellar models with MESA

We adopt the MESA mass-loss scheme and parameter setup introduced by S23¹, with some changes to enforce convergence until the formation of the CO core. In the following, we give an overview of our main parameters and initial conditions.

During the main sequence, we use the mass-loss framework described by Sabhahit et al. (2022) and extended to metal-poor stars by S23. This model describes the transition from an optically thin to an optically thick wind in VMSs (Vink et al. 2011; Bestenlehner et al. 2014), exploiting the concept of transition mass-loss rate (Vink & Gräfenor 2012). The transition happens when $\Gamma_{\text{Edd}} \geq \Gamma_{\text{Edd,tr}}$, where Γ_{Edd} is the Eddington ratio of a star

¹ We refer to the MESA inlists and run_star_extras files by S23, which are publicly available at this gitlab repository.

of luminosity L_* , defined as the ratio between L_* and the Eddington luminosity of the star, whereas $\Gamma_{\text{Edd,tr}}$ is the value of the Eddington ratio of the same star computed at the transition point. When stellar winds become optically thick, the mass-loss rate is enhanced according to Vink et al. (2011):

$$\dot{M} = \dot{M}_{\text{tr}} \left(\frac{L}{L_{\text{tr}}} \right)^{4.77} \left(\frac{M}{M_{\text{tr}}} \right)^{-3.99}, \quad (1)$$

where \dot{M}_{tr} , L_{tr} and M_{tr} are the mass-loss rate, the luminosity and the mass at the transition point. To obtain $\Gamma_{\text{Edd,tr}}$, the following condition is iteratively verified:

$$\eta^{\text{Vink}} \equiv \frac{\dot{M}_{\text{Vink}} v_{\infty}}{L/c} = \frac{\eta}{\tau_{F,s}} \left(\frac{v_{\infty}}{v_{\text{esc}}} \right) \sim \left(1 + \frac{v_{\text{esc}}^2}{v_{\infty}^2} \right)^{-1}, \quad (2)$$

where \dot{M}_{Vink} is the mass-loss rate computed following Vink et al. (2001), v_{∞} the asymptotical velocity, v_{esc} the escape velocity, η the wind efficiency of the model, and $\tau_{F,s}$ the flux-weighted mean optical depth. This condition allows to evaluate L_{tr} at each iteration, necessary to compute $\Gamma_{\text{Edd,tr}}$.

During the core He-burning phase, we use Eq. 1 only for temperatures between $4 \times 10^3 \text{ K}$ and 10^4 K , while for lower temperatures ($T < 4 \times 10^3 \text{ K}$), we follow de Jager et al. (1988). For $T > 10^4 \text{ K}$ and hydrogen mass fraction $X < 0.01$, we adopt the Wolf-Rayet (WR) mass-loss models by Sander & Vink (2020).

We treat convective mixing with the mixing length theory (MLT) by Cox & Giuli (1968), with a constant mixing-length ratio $\alpha_{\text{MLT}} = 1.5$. The convective boundaries are set by applying the Ledoux criterion (Ledoux 1947). We use the semi-convective diffusion parameter $\alpha_{\text{SC}} = 1$. We choose the exponential overshooting by Herwig (2000) to describe the overshooting above the convective regions with efficiency parameter $f_{\text{OV}} = 0.03$. We consider only non-rotating models. Finally, we turn on the MLT++ option (Paxton et al. 2013) only during the core He-burning phase to ensure convergence. MLT++ is an option that allows to reduce superadiabaticity ($\nabla_{\text{T}} > \nabla_{\text{ad}}$, where ∇_{T} is the temperature gradient and ∇_{ad} the adiabatic temperature gradient) in radiation-dominated convective regions with a-posteriori calculations. We refer to S23 for a more in-depth description of the parameters and the model.

We make exactly the same assumptions as S23 with only two exceptions: the definition of core boundaries and the nuclear reaction network. As for the core boundaries, we define the radius of the helium core as the radius inside which the mass fraction of hydrogen drops below $f_{\text{X}} = 10^{-4}$. Similarly, we define the radius of the helium (carbon) core as the radius inside which the mass fraction of ^4He (^{12}C) drops below $f_{\text{Y}} = 10^{-4}$ ($f_{\text{C}} = 10^{-4}$). The default of MESA instead sets the boundary of the H, He, and C core where the mass fraction of H, ^4He , and ^{12}C goes below 0.1, respectively. Our definition yields a more precise description of the core and is the same as assumed by the MIST libraries (Paxton et al. 2011, 2013, 2015; Dotter 2016; Choi et al. 2016).

We adopt the default nuclear reaction network in MESA with one exception: after the main sequence, we enable the `co_burn_net` (parameter `auto_extend_net = true`), which includes ^{28}Si , in order to have a more complete and extended network for C- and O-burning and α -chains with respect to S23.

We calculate stellar models with initial masses ranging from 50 to $500 M_{\odot}$ by intervals of $25 M_{\odot}$. The initial metallicities are $Z = 0.008, 0.006, 0.004, 0.002, 0.001, 0.0008, 0.0006, 0.0004, 0.0002,$ and 0.0001 . Thus, our grid consists of 190 models (19 initial masses and 10 initial metallicities). The initial helium mass fraction, Y , is computed as $Y = Y_{\text{prim}} + (\Delta Y / \Delta Z) Z$, where

Y_{prim} is the primordial helium abundance and $\Delta Y/\Delta Z$ describes the helium-to-metal ratio. We adopt the default values from MESA (Pols et al. 1998), with $Y_{\text{prim}} = 0.24$ and $\Delta Y/\Delta Z = 2$. This formulation spans the range from a nearly primordial composition ($X = 0.76$, $Y = 0.24$, $Z = 0$) to a quasi-solar one ($X = 0.70$, $Y = 0.28$, $Z = 0.02$). The hydrogen mass fraction is given by $X = 1 - Y - Z$.

We evolve all the stellar models until the luminosity due to carbon burning L_C is less than the 20% of the total luminosity L_{TOT} ($L_C/L_{\text{TOT}} < 0.2$) and the central He abundance is $Y_c < 10^{-8}$.

Figure 1 shows the mass-loss rate of our models for four selected metallicities, until the end of core He burning. During the main sequence, the initial mass required to enter the optically thick wind regime grows with decreasing metallicity: at $Z = 0.0008$, models with $M_{\text{ZAMS}} \leq 125 M_{\odot}$ do not experience optically thick winds, while at $Z = 0.008$ even the less massive models experience enhanced winds.

When stars that begin their life with $\Gamma_{\text{Edd}} < \Gamma_{\text{Edd, tr}}$ enter the optically thick wind regime, they experience a boost in the mass-loss. Instead, the mass-loss rate of stars that begin their life with $\Gamma_{\text{Edd}} > \Gamma_{\text{Edd, tr}}$ reaches a peak of $\sim 10^{-3.5} M_{\odot} \text{yr}^{-1}$ during the main sequence and then starts to decrease. We discuss other properties of our MESA stellar models in Appendix A.

2.2. Population synthesis with SEVN

We use the population-synthesis code SEVN (Spera & Mapelli 2017; Spera et al. 2019; Mapelli et al. 2020; Iorio et al. 2023)² to interpolate among our MESA models and estimate the (P)PISN rate density. SEVN evolves populations of single and binary stars by interpolating pre-computed stellar tracks and incorporating semi-analytic models for mass transfer, tides, supernova explosions, and gravitational-wave decay. We refer to Iorio et al. (2023) for a complete description of the code.

Here, we use the outputs from our new MESA models to obtain new evolutionary tables for stars with mass $M_{\star} \geq 50 M_{\odot}$.

We consider the same initial metallicities as in the MESA models. We simulate 10^5 stars for each metallicity. The initial masses are distributed following a Kroupa initial mass function (IMF, Kroupa 2001) with slope $\alpha = 2.3$ between $50 M_{\odot}$ and $500 M_{\odot}$. To model pair-instability and pulsational pair-instability supernovae, we use the fitting formulas described by Mapelli et al. (2020), based on the models by Woosley (2017). Namely, a star undergoes a PPISN if the final mass of the He core is between $32 M_{\odot} \leq M_{\text{He, f}} < 64 M_{\odot}$. A PISN takes place if $64 M_{\odot} \leq M_{\text{He, f}} \leq 135 M_{\odot}$. For higher masses of the He core, the star directly collapses onto an intermediate-mass BH. While a PISN leaves no compact remnant, the mass of the BH after a PPISN M_{PPISN} is estimated as

$$M_{\text{BH}} = \alpha_{\text{P}} M_{\text{CCSN}}, \quad (3)$$

where M_{CCSN} is the expected BH mass based on the fitting formulas by Fryer et al. (2012) and α_{P} is a correction factor depending on the mass of He-core and on the ratio between the He-core mass and the total mass in the pre-supernova stage.

As a comparison, we also consider the SEVN tables produced with the stellar evolution code PARSEC (Bressan et al. 2012; Chen et al. 2015; Costa et al. 2019a,b; Nguyen et al. 2022; Costa et al. 2025), and described by Iorio et al. (2023). The main difference

² We used the version 2.10.1 of SEVN, updated to commit hash c9dc8e4578990fd85cba91e082ebff6068388f56. SEVN is publicly available at this gitlab repository.

between the PARSEC and MESA models is that the former adopt a different stellar wind model from the one described by S23. The PARSEC wind model introduced by Chen et al. (2015, hereafter C15) is based on the fitting formulas by Vink et al. (2000) and Vink et al. (2001) for the winds of O-type stars, with additional corrections for electron scattering, and a dependence of the mass-loss on the Eddington ratio (Gräfener & Hamann 2008; Vink et al. 2011). We provide more details about the PARSEC models in Appendix B.

2.3. (P)PISN rate density evolution across cosmic time

We model the evolution of the (P)PISN rate density as a function of redshift with the code COSMORATE³ (Santoliquido et al. 2020, 2021), based on the observed metal-dependent cosmic star formation rate density (Madau & Fragos 2017).

The default version of COSMORATE estimates the merger rate density of compact binaries as a function of the redshift, but it can be adapted to trace the rate density of other transients of stellar origin, including (P)PISNe. Specifically, we calculate the rate of (P)PISNe as follows:

$$\mathcal{R}(z) = \int_{z_{\text{min}}}^z \left[\int_{z_{\text{min}}}^{z_{\text{max}}} \mathcal{S}(z', Z) \mathcal{F}(z', z, Z) dZ \right] \frac{dt(z')}{dz'} dz', \quad (4)$$

where $\mathcal{S}(z', Z) = \psi(z') p(z', Z)$.

Here, $\psi(z')$ is the cosmic star formation rate density at redshift z' , and $p(z', Z)$ is the distribution of metallicity Z at fixed formation redshift z' . In Equation 4, $dt(z')/dz' = H_0^{-1} (1 + z')^{-1} [(1 + z')^3 \Omega_{\text{M}} + \Omega_{\Lambda}]^{-1/2}$, where H_0 is the Hubble parameter, Ω_{M} and Ω_{Λ} are the matter and energy density, respectively. We adopt the values from Planck Collaboration et al. (2020).

The term $\mathcal{F}(z', z, Z)$ in Equation 4 is given by:

$$\mathcal{F}(z', z, Z) = \frac{1}{M_{\star}(z)} \frac{d\mathcal{N}(z', z, Z)}{dt(z)}, \quad (5)$$

where $d\mathcal{N}(z', z, Z)/dt(z)$ is the rate of (P)PISNe from stars with metallicity Z that formed at redshift z' and undergo a (P)PISN at redshift z , and $M_{\star}(z', Z)$ is the initial total stellar mass that forms at redshift z' with metallicity Z . We obtain $d\mathcal{N}(z', z, Z)/dt(z)$ directly from our simulations.

We model the star formation rate density through the fitting formula by Harikane et al. (2022):

$$\psi(z) = \left[61.7(1 - z)^{-3.13} + 10^{0.22(1+z)} + 2.4^{0.5(1+z)-3} \right]^{-1} \frac{M_{\odot}}{\text{Mpc}^3 \text{yr}}. \quad (6)$$

They obtained this formula through the analysis of new measurements of the rest-frame UV luminosity at $z \sim 4 - 7$ based on wide and deep optical images obtained in the Hyper Suprime Cam (HSC) Subaru Strategic Program (SSP) survey (Aihara et al. 2018) and the CFHT Large Area U-band Deep Survey (CLAUDS; Sawicki et al. 2019). This formula is a better match to recent James Webb Space Telescope (JWST) data (Donnan et al. 2023; Harikane et al. 2023, 2024) than the traditionally adopted fit by Madau & Dickinson (2014). The star formation rate density is then multiplied by a correction factor $f_{\text{Kroupa}} = 0.66$ to convert the SFR from a Salpeter IMF to a Kroupa IMF (Madau & Dickinson 2014).

The metallicity-evolution term $p(z', Z)$ is the probability density function that a star formed at redshift z' has a metallicity

³ COSMORATE is publicly available at this gitlab repository.

Z , modelled as a log-normal distribution function (Chruslinska et al. 2019; Santoliquido et al. 2023):

$$p(z', Z) = \frac{1}{\sqrt{2\pi\sigma_Z^2}} \exp\left\{-\frac{[\log(Z/Z_\odot) - \langle \log(Z/Z_\odot) \rangle]^2}{2\sigma_Z^2}\right\}. \quad (7)$$

We derive $\langle \log(Z/Z_\odot) \rangle$ from the fitting formula by Madau & Fragos (2017)

$$\log\langle Z/Z_\odot \rangle = 0.153 - 0.074 z^{1.34}, \quad (8)$$

knowing that $\langle \log Z/Z_\odot \rangle = \log\langle Z/Z_\odot \rangle - \ln(10)\sigma_Z^2/2$. We assume $\sigma_Z = 0.4$, based on the results by Sgalletta et al. (2024).

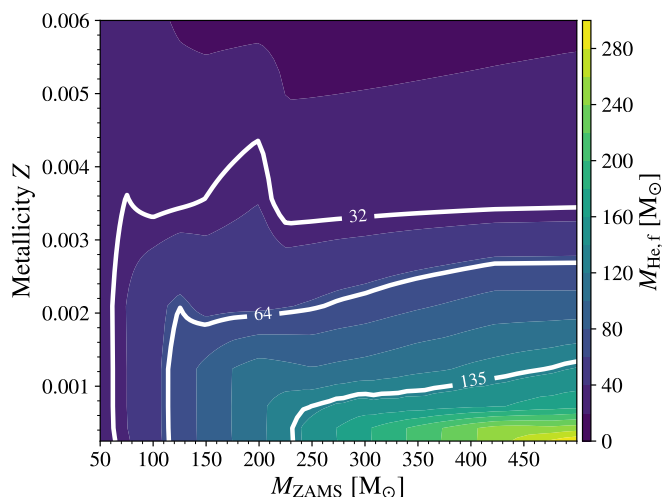


Fig. 2: Contour plot showing the He core masses at the end of the He burning for our MESA tracks adopting S23 winds as a function of the metallicity and ZAMS mass. The white lines highlight the levels at $32M_\odot$, $64M_\odot$ and $135M_\odot$, which set the boundaries to have PPISNe, PISNe, and direct collapse via photodisintegration.

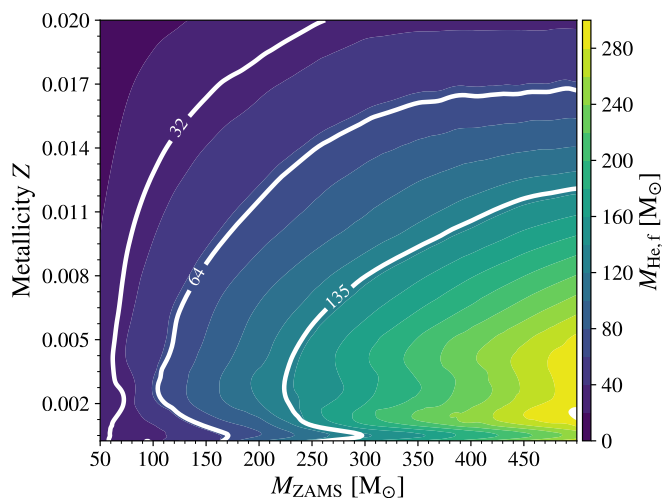


Fig. 3: Same as Fig. 2, but for models C15.

3. Results

3.1. The metallicity threshold for (P)PISNe

Figure 2 shows the final helium core mass for our MESA models with S23 winds as a function of metallicity and ZAMS mass. We highlight the levels corresponding to $M_{\text{He,f}} = 32, 64,$ and $135 M_\odot$, because these correspond to the threshold for PPISN, PISN, and direct collapse according to Woosley (2017). In the S23 model, the maximum He core mass of stars with M_{ZAMS} up to $500 M_\odot$ is below $65 M_\odot$ for metallicity $Z \gtrsim 0.003$ and below $135 M_\odot$ for $Z \gtrsim 0.0015$.

Assuming that the He core mass is a good proxy for the onset of pair instability and adopting the models by Woosley (2017), the results presented in Figs. 2 and 3 allow us to estimate the threshold metallicity for the onset of (P)PISNe for both the S23 and C15 models. With our new models (S23), the maximum metallicity for PISNe and PPISNe are $Z \sim 2 \times 10^{-3}$ and $Z \sim 4.5 \times 10^{-3}$, respectively. For comparison, the model adopting the PARSEC stellar tracks (C15) yields $Z \sim 1.7 \times 10^{-2}$ and $Z \gtrsim 2 \times 10^{-2}$ as thresholds for PISNe and PPISNe, respectively (Fig. 3). Such metallicities are extremely high, above the solar value ($Z \sim 0.015$, e.g., Caffau et al. 2011).

In the S23 model (Fig. 2), even stars whose initial mass is higher than $250 M_\odot$ explode as PISNe if their metallicity lies between 0.001 and 0.002. At lower metallicities, stars with ZAMS mass $> 250 M_\odot$ collapse directly to black holes, because photodisintegration prevents the explosion, while stars with ZAMS mass between 110 and $230 M_\odot$ undergo PISNe. Stars with $64 M_\odot \leq M_{\text{ZAMS}} \leq 110 M_\odot$ undergo PPISN for $Z \leq 0.004$ and this mass range extends up to $M_{\text{ZAMS}} = 500 M_\odot$ for $0.002 \leq Z \leq 0.004$.

Figure 4 shows the evolution of the He core mass at the end of core He burning for some selected metallicities, comparing S23 and C15. From this Figure, it is apparent how the onset of optically thick winds during the main sequence progressively "erodes" the core of the most massive stars for $Z \geq 0.0004$ in our MESA models. In contrast, the PARSEC models grow large cores even at relatively high metallicity ($Z \geq 0.0004$) because of the different wind model.

However, at low metallicities ($Z \lesssim 0.0004$), the PARSEC models tend to develop smaller cores than the MESA models for ZAMS masses $M_{\text{ZAMS}} \geq 80 M_\odot$. This difference arises from the different envelope undershooting and convection models adopted by MESA and PARSEC (see Appendices A and B), rather than by the wind model. Specifically, the PARSEC tracks develop effective dredge-up episodes that exchange mass between the envelope and the He core, reducing the overall He core mass at the end of core He burning (Costa et al. 2021).

3.2. (P)PISN rate density

Figure 5 shows the evolution of the PISN and PPISN rate density across cosmic time. We compare our new MESA models adopting the mass-loss rate by S23 to the PARSEC models with the mass-loss rate presented by C15. We also compare the models with the observational constraints reported by Schulze et al. (2024).

At low redshift, the (P)PISN rate density of the S23 model is lower by two orders of magnitude compared to the C15 model (see Tab. 1). The PISN rate of the S23 model is below the observational upper limit set by Schulze et al. (2024), whereas the C15 model yields a much higher rate than the upper limit.

The main reason for this difference is that the metallicity threshold to activate the PISNe is lower in the S23 model

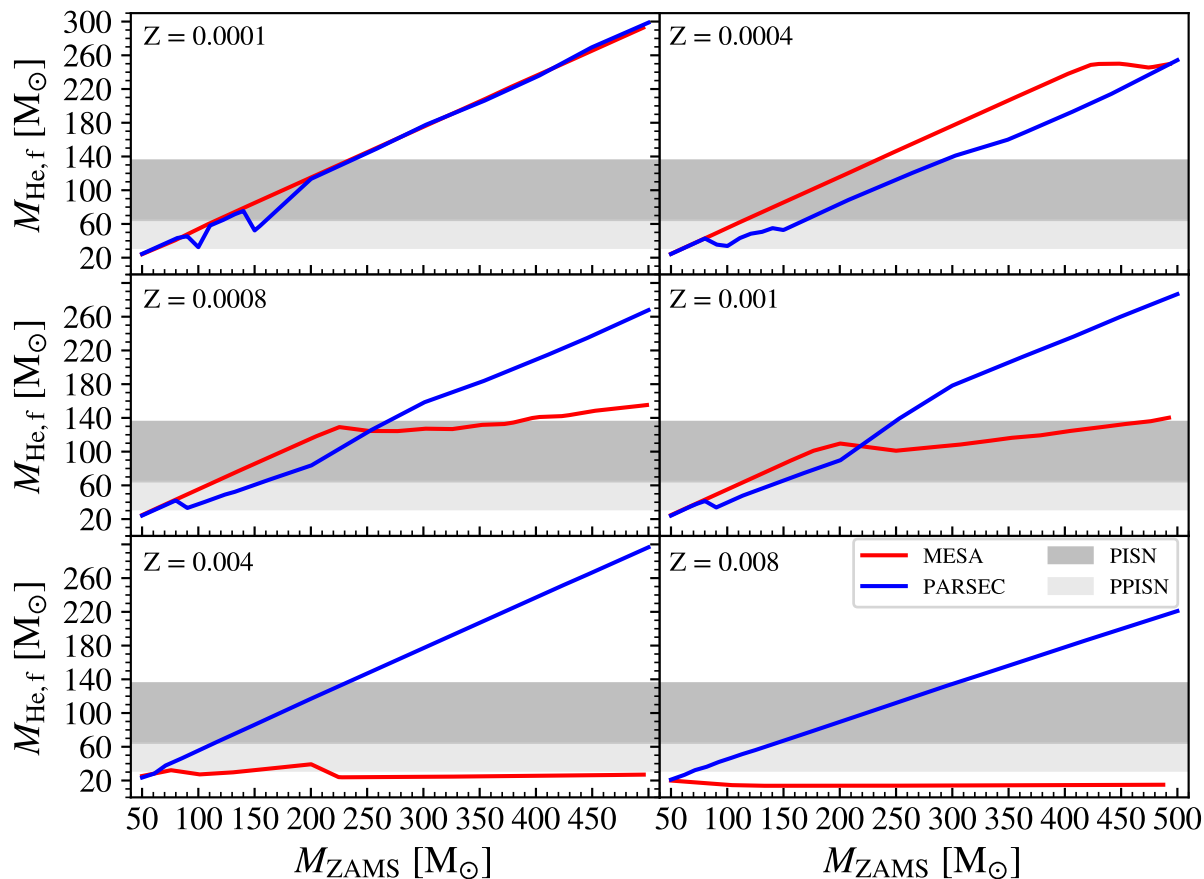


Fig. 4: Final helium core mass as a function of the ZAMS mass. The red lines are our new MESA tracks (models S23), while the blue lines correspond to results from PARSEC tracks (models C15). Dark (Light) gray shaded areas: regime for PISNe (PPISNe). From top left to bottom right we show metallicities $Z = 0.0001, 0.0004, 0.0008, 0.001, 0.004, 0.008$.

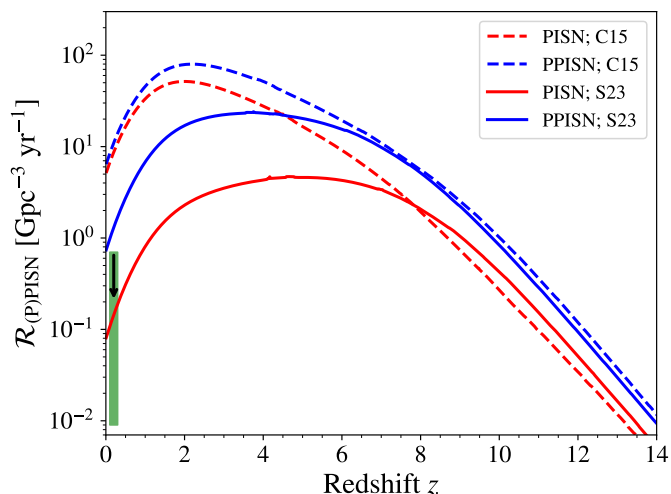


Fig. 5: PISN (red lines) and PPISN (blue lines) rate densities as a function of redshift. The solid and dashed lines are obtained using the model by S23 and C15, respectively. The green shaded area represents the observational constraints set by Schulze et al. (2024). The black arrow highlights the upper limit from Schulze et al. (2024).

($Z \leq 0.002$) than in the C15 model ($Z \leq 0.017$), as shown in Figs. 2 and 3. According to the C15 model, we expect PISNe to take place even at the metallicity of the Small ($Z \approx 0.003$) and Large Magellanic Clouds ($Z \approx 0.008$), whereas the S23 model predicts that PISNe only take place at metallicities lower than the one of the Small Magellanic Cloud.

At high redshift, the main contribution to the PISN rate comes from very metal-poor stars ($Z < 0.002$), for which the mass-loss rates adopted in the S23 and C15 models behave almost in the same way (Fig. 6). However, the (P)PISN rates obtained with models S23 and C15 show some differences even at high redshift. Specifically, at redshift $z \geq 8$, the rate of the S23 model becomes slightly higher than the rate of the C15 models. This happens because of other differences between the MESA and PARSEC stellar tracks that we already discussed in Section 3.1. Specifically, Fig. 4 shows that the final He core mass of the PARSEC tracks (C15) at metallicity $0.0001 \leq Z \leq 0.0006$ tends to be lower than the one of the MESA tracks (Sabahit et al. 2023), reducing the overall PISN rate in the C15 models.

3.3. The impact of metallicity evolution

Figure 6 shows the contribution of various metallicities to the (P)PISN rate for our two models. Below redshift $z = 5$, the two models behave in a completely different way: if we assume the winds by Sabahit et al. (2023) the main contribution to PISNe

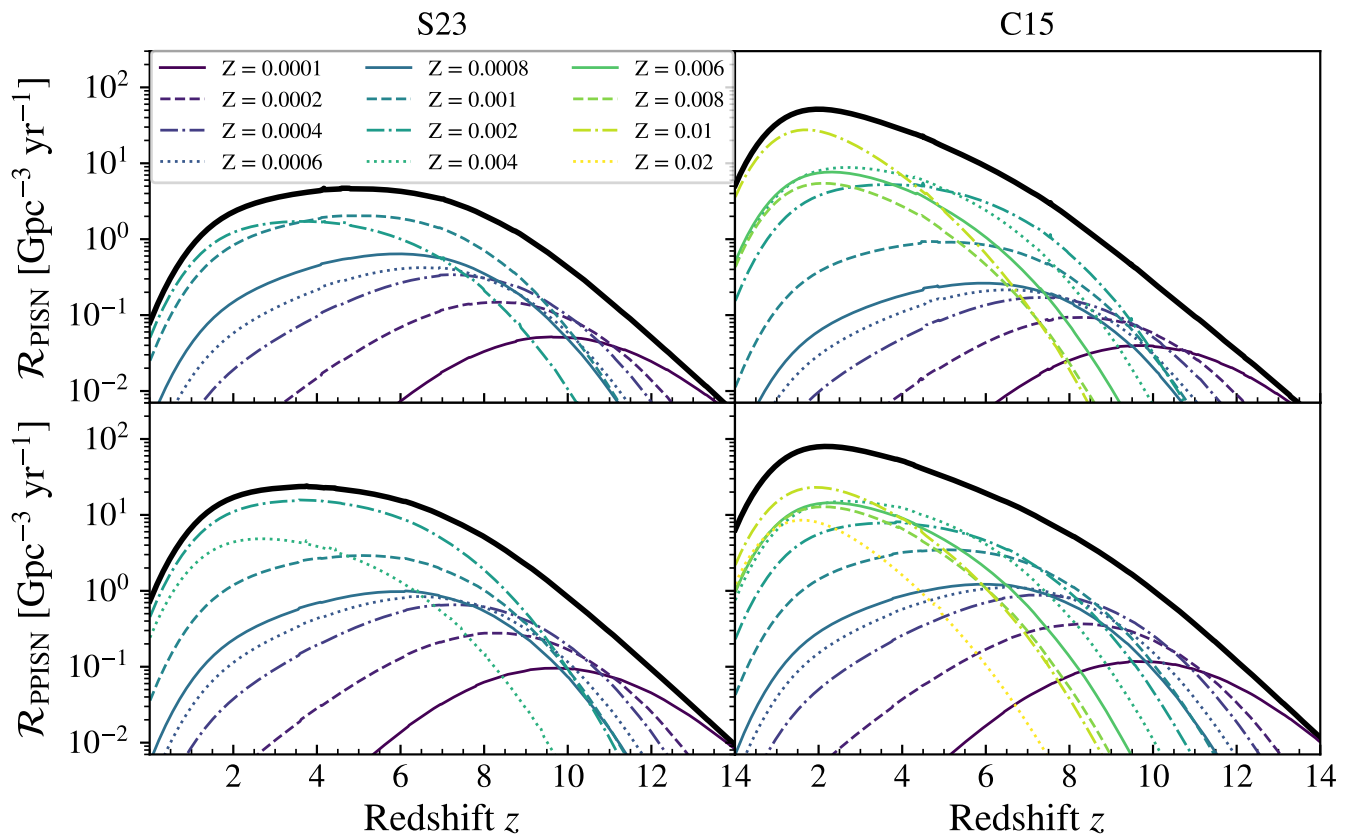


Fig. 6: PISN (upper panels) and PPISN (lower panels) rate density evolution as a function of redshift. The left-hand and right-hand plots show the results obtained with the new wind model by [S23](#) and the one by [C15](#), respectively. The black thick line represents the total rate density, whereas the colored lines show the contribution of individual metallicities from $Z = 1 \times 10^{-4}$ (violet solid line) to $Z = 2 \times 10^{-2}$ (dashed yellow line).

(PPISNe) comes from metallicity $Z = 0.001$ – 0.002 ($Z = 0.002$), whereas if we adopt the winds by [Chen et al. \(2015\)](#) the dominant metallicity is $Z = 0.01$ for both PISNe and PPISNe. At $z > 5$, the two models evolve in a more similar way and also lower metallicities become important.

Figure 6 assumes our fiducial metallicity spread $\sigma_Z = 0.4$ (see Eq. 7). In Figure 7, we show the impact of the parameter σ_Z on our results. Specifically, we change the metallicity spread σ_Z between 0.1 and 0.6.

In the results based on models [C15](#), the rates are mainly influenced by medium-to-high metallicities with a peak at $z \sim 2$ determined by metallicity $Z = 0.01$ (see also Fig. 6). As a consequence, changing σ_Z has little effect, introducing only minor fluctuations at redshift $z = 7$ for (P)PISN rate density, and leading to PPISN rate densities at $z = 0$ that range from 2 to $8.5 \text{ yr}^{-1} \text{ Gpc}^{-3}$. This occurs because of the high metallicity threshold for PISN in [C15](#) models. In this case, the rate density is dominated by the peak of the SFRD, with the spread of the metallicity playing only a minor role ([Gabrielli et al. 2024](#)). As a result, the rate is almost insensitive to σ_Z .

In contrast, when enhanced winds are considered, there is no contribution from metallicities $Z > 2 \times 10^{-3}$ for PISNe ($Z > 4 \times 10^{-3}$ for PPISNe). This leads to a strong dependence on metallicity evolution, allowing the PISN rate to be always below the upper limit estimated by [Schulze et al. \(2024\)](#), even when $\sigma_Z \sim 0.5$. The PISN rate density at redshift $z = 0$ even falls below the lower limit set by [Schulze et al. \(2024\)](#) when assum-

ing $\sigma_Z < 0.3$. In this case, a different value of σ_Z shifts also the expected peak from $z \sim 7$ (assuming $\sigma_Z = 0.1$) to $z \sim 2$ (assuming $\sigma_Z = 0.6$). These results depend on our simplifying assumption that the distribution of metallicities at a given redshift follows a log-normal distribution around the mean value. We will study more detailed distributions in a follow-up study. Model [C15](#) is almost unaffected by the spread σ_Z because the threshold metallicity for (P)PISNe is so high that there is always a subpopulation of VMSs that end their life with a (P)PISN, even at low redshift. The rate becomes then more sensitive to the IMF (maximum stellar mass and slope of the mass function) than to the metallicity spread.

4. Discussion

The stellar wind model proposed by [S23](#) has a strong impact on the evolution of VMSs. The high mass-loss rate in the optically thick regime causes the most massive stars at metallicity $Z \geq 0.004$ to end their life with a He core mass lower than $32 M_\odot$, without entering the (pulsational) pair-instability regime. In contrast, at metallicity $Z = 0.001$, even stars with masses between 250 and $500 M_\odot$ can undergo PISNe. This has important consequences on the expected mass function of black holes (Tornamenti et al., in prep.). Here, we have found that the enhanced mass-loss rate lowers the maximum metallicity for PISNe from $Z \sim 1.7 \times 10^{-2}$ to $Z \sim 2 \times 10^{-3}$, as also shown by [S23](#). The absence of contributions by higher metal-

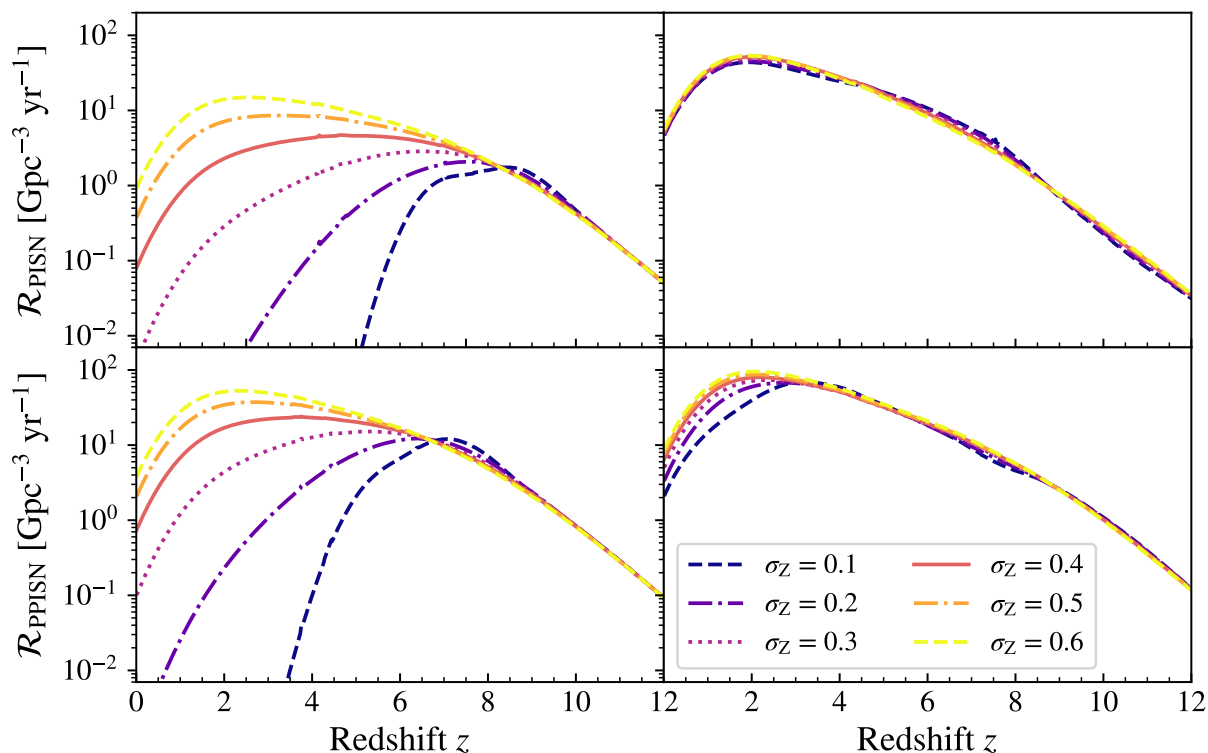


Fig. 7: PISN (upper row) and PPISN (lower row) as a function of the redshift, varying the metallicity spread from $\sigma_Z = 0.1$ (dark blue dashed line) to $\sigma_Z = 0.6$ (yellow dashed line). Left-hand (right-hand) panels: models with stellar winds from S23 (from C15).

Model	$\mathcal{R}_{\text{PISN}, z=0}$ [$\text{yr}^{-1} \text{Gyr}^{-3}$]	$\mathcal{R}_{\text{PPISN}, z=0}$ [$\text{yr}^{-1} \text{Gyr}^{-3}$]
This work (S23 winds)	8×10^{-2}	0.8
This work (C15 winds)	5.8	6.5
B22 (empirical)	6.6	
B22 (EAGLE)	0.8	
B22 (ILLUSTRISTNG)	1.3	
B22 (MILLENNIUM)	5.1	
T23 (fiducial)	1.7	
T23 (-3σ)	0.02	
G24 ($\tilde{\sigma}_Z = 0.15, Z_{\text{th}} = 0.0015$)	3×10^{-4}	
G24 ($\tilde{\sigma}_Z = 0.35, Z_{\text{th}} = 0.0015$)	1.2	
G24 ($\tilde{\sigma}_Z = 0.70, Z_{\text{th}} = 0.0015$)	22	
G24 ($Z_{\text{th}} = 0.017$)	1970	

Table 1: PISN and PPISN rate density at redshift $z = 0$ from B22, T23, and G24). For B22, models Empirical, EAGLE, ILLUSTRISTNG and MILLENNIUM refer to different models for the star formation rate density evolution. For T23, models fiducial and -3σ assume different rates of the $^{12}\text{C}(\alpha, \gamma)^{16}\text{O}$ reaction. The different values reported for G24 assume three different values of the metallicity dispersion $\tilde{\sigma}_Z$ and two different metallicity threshold for PISN Z_{th} .

licities suppresses the predicted peak of the PISN rate at redshift $z \sim 2$ and reduces the expected rate at redshift $z = 0$ by two orders of magnitude compared to the PARSEC stellar tracks (C15). The PISN rate density of our MESA models falls within

the observational constraints estimated by Schulze et al. (2024): $0.009 \text{ Gpc}^{-3} \text{ yr}^{-1} \leq \mathcal{R}_{\text{PISN}} \leq 0.7 \text{ Gpc}^{-3} \text{ yr}^{-1}$.

To better comprehend the critical impact of stellar winds and metallicity on the (P)PISN rate, we compare our results with previous works. B22 demonstrated that the variation of the star formation rate model widely affects the PISN rate. Their empirical model aligns with our results from model C15, showing a peak around $z \sim 2$ and a similar value at $z = 0$ of approximately $\mathcal{R}_{\text{PISN}} \sim 6 \text{ yr}^{-1} \text{ Gyr}^{-3}$. In the other models they considered the PISN rate peak is at $z \sim 3$, resulting in a lower rate at $z = 0$, but still exceeding the more recent observational constraints.

T23 explored the impact of variations in the $^{12}\text{C}(\alpha, \gamma)^{16}\text{O}$ reaction rate, predicting a peak of the PISN rate around $z \sim 6$. This higher redshift may be attributed to the different metallicity distribution they assumed. As already discussed by G24, binary interactions are not expected to significantly impact the predicted rate. Moreover, the inclusion of enhanced stellar winds can lead to wider binaries due to the large amount of mass ejected, reducing the effects of binary evolution.

G24 also investigated how metallicity evolution influences the expected PISN rate. They assumed the metallicity distributed as a log-normal distribution around the fundamental metallicity relation (FMR; Curti et al. 2020) with a metallicity spread $\tilde{\sigma}_Z$. Changing $\tilde{\sigma}_Z$ from 0.15 to 0.7 and the maximum metallicity to have PISN Z_{th} from 1.5×10^{-3} to 1.7×10^{-2} , they observed a change of several orders of magnitude in the PISN rate, largely exceeding the upper limits by Schulze et al. (2024) when $\tilde{\sigma}_Z \geq 0.35$ and $Z_{\text{th}} \geq 1.5 \times 10^{-3}$. In our work, the metallicity spread σ_Z is defined as the standard deviation of a log-normal distribution around the average metallicity evolution of stars (Eq. 7). Hence, it is not directly comparable with the parameter $\tilde{\sigma}_Z$ adopted by G24, even if both parameter quantify the

dispersion of the stellar metallicity distribution (see the discussion by Sgalletta et al. 2024).

As shown in the left-hand panels of Fig. 7, the PISN rates of our MESA models are also very sensitive to metallicity, but, considering $\sigma_Z \leq 0.5$, the results are consistent with the observational upper limit. We do not expect that a more detailed modeling of metallicity evolution would affect our results. Indeed, since the S23 models do not include contributions from high metallicities, the high-metallicity tail predicted by the log-normal distribution of Z has no impact on the outcome.

A summary of all PISN rate densities at $z = 0$ discussed here is provided in Table 1.

5. Summary

Here, we have studied the impact of the new stellar wind model by S23 on the rate of pair-instability supernovae (PISNe) and pulsational pair-instability supernovae (PPISNe), by integrating new very massive star (VMS) tracks with MESA (Paxton et al. 2019) and by convolving our results with a metal-dependent star formation history (Santoliquido et al. 2021).

The model by S23 describes the transition from optically thin to optically thick winds resulting in high mass-loss rates ($\dot{M} \gtrsim 10^{-4} M_\odot$) already during the main sequence of VMSs, for metallicities $Z \gtrsim 0.0004$. This quenches the growth of VMS' cores (Fig. 4) and prevents the onset of PISNe at metallicity $Z \geq 2 \times 10^{-3}$, even if we assume a maximum ZAMS mass as high as $500 M_\odot$ (S23).

We find that the PISN (PPISN) rate density at $z = 0$ is $\mathcal{R}_{\text{PISN}} = 0.08 \text{ Gpc}^{-3} \text{ yr}^{-1}$ ($\mathcal{R}_{\text{PPISN}} = 0.8 \text{ Gpc}^{-3} \text{ yr}^{-1}$) for the S23 wind model, if we assume a metallicity dispersion $\sigma_Z = 0.4$ (Fig. 6 and Table 1). By changing the metallicity dispersion σ_Z from 0.1 to 0.6, the local (P)PISN rate density changes by several orders of magnitude (Fig. 7), because it is extremely sensitive to the fraction of star formation that occurs above the metallicity threshold for (P)PISNe.

For $\sigma_Z = 0.4 - 0.5$, our expected local PISN rate density ($\mathcal{R}_{\text{PISN}, z=0} = 0.08 - 0.4 \text{ Gpc}^{-3} \text{ yr}^{-1}$) is consistent with the observational constraints ($0.009 < \mathcal{R}_{\text{PISN}}/\text{Gpc}^{-3} \text{ yr}^{-1} < 0.7$) inferred by Schulze et al. (2024). Notably, this result does not require to cap the maximum stellar mass or to assume an unrealistically thin metallicity dispersion.

In our S23 models, the PISN rate density grows up to a few $\times \text{Gpc}^{-3} \text{ yr}^{-1}$ at redshift $z = 2 - 6$. The main contribution to PISNe and PPISNe comes from stars with metallicity $Z = 0.001 - 0.002$.

We have compared our new MESA models with the PARSEC stellar tracks reported by Costa et al. (2025), adopting the fitting formulas by Vink et al. (2001) for O-type stars, with corrections for electron scattering introduced by C15. The PARSEC tracks lead to a higher maximum metallicity ($Z \geq 1.7 \times 10^{-2}$) for PISNe if we assume the same maximum ZAMS mass. As a consequence, the PISN rate density at $z = 0$ is much higher ($\sim 6 \text{ Gpc}^{-3} \text{ yr}^{-1}$), above the observational upper limit.

Our results confirm the importance of stellar winds to describe the evolution of VMSs, the rate of (P)PISNe, and the expected mass function of black holes (Torniamenti et al., in prep.).

Acknowledgements. We wholeheartedly thank Gautham Sabahit and collaborators for sharing their MESA inlists (https://github.com/Apophis-1/VMS_Paper1, https://github.com/Apophis-1/VMS_Paper2). Our work would not have been possible without this invaluable open-science input. We thank Marco Dall'Amico, Varsha Ramachandran, Andreas Sander, Raffaele Scala and Jorick Vink for useful discussions. MM, GI, and ST acknowledge financial support from the European Research Council for the ERC Consolidator grant DEMOBLACK, under contract no. 770017. MM and ST also acknowledge finan-

cial support from the German Excellence Strategy via the Heidelberg Cluster of Excellence (EXC 2181 - 390900948) STRUCTURES. ST acknowledges financial support from the Alexander von Humboldt Foundation for the Humboldt Research Fellowship. GI acknowledges financial support from the La Caixa Foundation for the La Caixa Junior Leader fellowship 2024. GI also acknowledges financial support under the National Recovery and Resilience Plan (NRRP), Mission 4, Component 2, Investment 1.4, - Call for tender No. 3138 of 18/12/2021 of Italian Ministry of University and Research funded by the European Union - NextGenerationEU. The authors acknowledge support by the state of Baden-Württemberg through bwHPC and the German Research Foundation (DFG) through grants INST 35/1597-1 FUGG and INST 35/1503-1 FUGG. We use the MESA software (<https://docs.mesastar.org/en/latest/>) version r12115; (Paxton et al. 2011, 2013, 2015, 2018, 2019). We used SEVN (<https://gitlab.com/sevncodes/sevn>) to generate our BBHs catalogs (Spera et al. 2019; Mapelli et al. 2020; Iorio et al. 2023). We used TRACKCRUNCHER (<https://gitlab.com/sevncodes/trackcruncher>) (Iorio et al. 2023) to produce the tables needed for the interpolation in SEVN. We used COSMORATE (https://gitlab.com/Filippo.santoliquido/cosmo_rate_public) (Santoliquido et al. 2020, 2021) to compute the rate densities. This research made use of NUMPY (Harris et al. 2020), SCIPY (Virtanen et al. 2020), PANDAS (The pandas development Team 2024). For the plots we used MATPLOTLIB (Hunter 2007).

References

- Aihara, H., Arimoto, N., Armstrong, R., et al. 2018, PASJ, 70, S4
 Barkat, Z., Rakavy, G., & Sack, N. 1967, Phys. Rev. Lett., 18, 379
 Belkus, H., Van Bever, J., & Vanbeveren, D. 2007, ApJ, 659, 1576
 Bestenlehner, J. M., Crowther, P. A., Caballero-Nieves, S. M., et al. 2020, MNRAS, 499, 1918
 Bestenlehner, J. M., Gräfener, G., Vink, J. S., et al. 2014, A&A, 570, A38
 Boco, L., Lapi, A., Goswami, S., et al. 2019, ApJ, 881, 157
 Böhm-Vitense, E. 1958, ZAp, 46, 108
 Bond, J. R., Arnett, W. D., & Carr, B. J. 1984, ApJ, 280, 825
 Bressan, A., Marigo, P., Girardi, L., et al. 2012, MNRAS, 427, 127
 Bressan, A. G., Chiosi, C., & Bertelli, G. 1981, A&A, 102, 25
 Briel, M. M., Eldridge, J. J., Stanway, E. R., Stevance, H. F., & Chrimes, A. A. 2022, MNRAS, 514, 1315
 Briel, M. M., Metha, B., Eldridge, J. J., Moriya, T. J., & Trenti, M. 2024, MNRAS, 533, 3907
 Brott, I., de Mink, S. E., Cantiello, M., et al. 2011, A&A, 530, A115
 Caffau, E., Ludwig, H. G., Steffen, M., Freytag, B., & Bonifacio, P. 2011, Sol. Phys., 268, 255
 Cameron, A. J., Katz, H., Rey, M. P., & Saxena, A. 2023, MNRAS, 523, 3516
 Charbonnel, C., Schaerer, D., Prantzos, N., et al. 2023, A&A, 673, L7
 Chen, K.-J., Woosley, S., Heger, A., Almgren, A., & Whalen, D. J. 2014, ApJ, 792, 28
 Chen, Y., Bressan, A., Girardi, L., et al. 2015, MNRAS, 452, 1068
 Choi, J., Dotter, A., Conroy, C., et al. 2016, ApJ, 823, 102
 Chruslinska, M., Nelemans, G., & Belczynski, K. 2019, MNRAS, 482, 5012
 Cooke, J., Sullivan, M., Gal-Yam, A., et al. 2012, Nature, 491, 228
 Costa, G., Ballone, A., Mapelli, M., & Bressan, A. 2022, MNRAS, 516, 1072
 Costa, G., Bressan, A., Mapelli, M., et al. 2021, MNRAS, 501, 4514
 Costa, G., Girardi, L., Bressan, A., et al. 2019a, A&A, 631, A128
 Costa, G., Girardi, L., Bressan, A., et al. 2019b, MNRAS, 485, 4641
 Costa, G., Mapelli, M., Iorio, G., et al. 2023, MNRAS, 525, 2891
 Costa, G., Shepherd, K. G., Bressan, A., et al. 2025, A&A, 694, A193
 Cox, J. P. & Giuli, R. T. 1968, Principles of stellar structure
 Crain, R. A., Schaye, J., Bower, R. G., et al. 2015, MNRAS, 450, 1937
 Crowther, P. A., Schnurr, O., Hirschi, R., et al. 2010, MNRAS, 408, 731
 Curti, M., Mannucci, F., Cresci, G., & Maiolino, R. 2020, MNRAS, 491, 944
 de Jager, C., Nieuwenhuijden, H., & van der Hucht, K. A. 1988, Bulletin d'Information du Centre de Donnees Stellaires, 35, 141
 Donnan, C. T., McLeod, D. J., Dunlop, J. S., et al. 2023, MNRAS, 518, 6011
 Dotter, A. 2016, ApJS, 222, 8
 du Buisson, L., Marchant, P., Podsiadlowski, P., et al. 2020, MNRAS, 499, 5941
 Ebisuzaki, T., Makino, J., Tsuru, T. G., et al. 2001, ApJ, 562, L19
 Eldridge, J. J., Stanway, E. R., Xiao, L., et al. 2017, PASA, 34, e058
 Farag, E., Renzo, M., Farmer, R., Chidester, M. T., & Timmes, F. X. 2022, ApJ, 937, 112
 Farmer, R., Renzo, M., de Mink, S. E., Fishbach, M., & Justham, S. 2020, ApJ, 902, L36
 Farmer, R., Renzo, M., de Mink, S. E., Marchant, P., & Justham, S. 2019, ApJ, 887, 53
 Farrell, E., Groh, J. H., Hirschi, R., et al. 2021, MNRAS, 502, L40
 Fraley, G. S. 1968, Ap&SS, 2, 96
 Fremling, C., Miller, A. A., Sharma, Y., et al. 2020, ApJ, 895, 32
 Fryer, C. L., Belczynski, K., Wiktorowicz, G., et al. 2012, ApJ, 749, 91
 Gabrielli, F., Lapi, A., Boco, L., et al. 2024, MNRAS, 534, 151

- Gal-Yam, A., Mazzali, P., Ofek, E. O., et al. 2009, *Nature*, 462, 624
- Georgy, C., Ekström, S., Eggenberger, P., et al. 2013, *A&A*, 558, A103
- Gieles, M., Padoan, P., Charbonnel, C., Vink, J. S., & Ramírez-Galeano, L. 2025, arXiv e-prints, arXiv:2501.12138
- Giersz, M., Leigh, N., Hupki, A., Lützgendorf, N., & Askar, A. 2015, *MNRAS*, 454, 3150
- Goswami, S., Silva, L., Bressan, A., et al. 2022, *A&A*, 663, A1
- Gräfener, G. & Hamann, W. R. 2008, *A&A*, 482, 945
- Gräfener, G., Vink, J. S., de Koter, A., & Langer, N. 2011, *A&A*, 535, A56
- Harikane, Y., Nakajima, K., Ouchi, M., et al. 2024, *ApJ*, 960, 56
- Harikane, Y., Ono, Y., Ouchi, M., et al. 2022, *ApJS*, 259, 20
- Harikane, Y., Ouchi, M., Oguri, M., et al. 2023, *ApJS*, 265, 5
- Harris, C. R., Millman, K. J., van der Walt, S. J., et al. 2020, *Nature*, 585, 357
- Heger, A. & Woosley, S. E. 2002, *ApJ*, 567, 532
- Hendriks, D. D., van Son, L. A. C., Renzo, M., Izzard, R. G., & Farmer, R. 2023, *MNRAS*, 526, 4130
- Herwig, F. 2000, *A&A*, 360, 952
- Hirschi, R. 2015, in *Astrophysics and Space Science Library*, Vol. 412, *Very Massive Stars in the Local Universe*, ed. J. S. Vink, 157
- Hunter, J. D. 2007, *Computing in Science and Engineering*, 9, 90
- Iorio, G., Mapelli, M., Costa, G., et al. 2023, *MNRAS*, 524, 426
- Kojima, T., Ouchi, M., Rauch, M., et al. 2021, *ApJ*, 913, 22
- Kozyreva, A. & Blinnikov, S. 2015, *MNRAS*, 454, 4357
- Kozyreva, A., Kromer, M., Noebauer, U. M., & Hirschi, R. 2018, *MNRAS*, 479, 3106
- Kroupa, P. 2001, *MNRAS*, 322, 231
- Langer, N., Norman, C. A., de Koter, A., et al. 2007, *A&A*, 475, L19
- Ledoux, P. 1947, *ApJ*, 105, 305
- Leung, S.-C., Nomoto, K., & Blinnikov, S. 2019, *ApJ*, 887, 72
- Limongi, M. & Chieffi, A. 2018, *ApJS*, 237, 13
- Madau, P. & Dickinson, M. 2014, *ARA&A*, 52, 415
- Madau, P. & Fragos, T. 2017, *ApJ*, 840, 39
- Mapelli, M. 2016, *MNRAS*, 459, 3432
- Mapelli, M., Spera, M., Montanari, E., et al. 2020, *ApJ*, 888, 76
- Marchant, P. & Moriya, T. J. 2020, *A&A*, 640, L18
- Marinacci, F., Vogelsberger, M., Pakmor, R., et al. 2018, *MNRAS*, 480, 5113
- Mazzali, P. A., Moriya, T. J., Tanaka, M., & Woosley, S. E. 2019, *MNRAS*, 484, 3451
- Naiman, J. P., Pillepich, A., Springel, V., et al. 2018, *MNRAS*, 477, 1206
- Nelson, D., Pillepich, A., Springel, V., et al. 2018, *MNRAS*, 475, 624
- Nguyen, C. T., Costa, G., Girardi, L., et al. 2022, *A&A*, 665, A126
- Ohkubo, T., Umeda, H., Maeda, K., et al. 2006, *ApJ*, 645, 1352
- Paxton, B., Bildsten, L., Dotter, A., et al. 2011, *ApJS*, 192, 3
- Paxton, B., Cantiello, M., Arras, P., et al. 2013, *ApJS*, 208, 4
- Paxton, B., Marchant, P., Schwab, J., et al. 2015, *ApJS*, 220, 15
- Paxton, B., Schwab, J., Bauer, E. B., et al. 2018, *ApJS*, 234, 34
- Paxton, B., Smolec, R., Schwab, J., et al. 2019, *ApJS*, 243, 10
- Perley, D. A., Fremling, C., Sollerman, J., et al. 2020, *ApJ*, 904, 35
- Pillepich, A., Nelson, D., Hernquist, L., et al. 2018, *MNRAS*, 475, 648
- Planck Collaboration, Aghanim, N., Akrami, Y., et al. 2020, *A&A*, 641, A6
- Pols, O. R., Schröder, K.-P., Hurley, J. R., Tout, C. A., & Eggleton, P. P. 1998, *MNRAS*, 298, 525
- Portegies Zwart, S. F., Baumgardt, H., Hut, P., Makino, J., & McMillan, S. L. W. 2004, *Nature*, 428, 724
- Portegies Zwart, S. F., Dewi, J., & Maccarone, T. 2005, *Ap&SS*, 300, 247
- Portegies Zwart, S. F. & McMillan, S. L. W. 2002, *ApJ*, 576, 899
- Quimby, R. M., Gal-Yam, A., Arcavi, I., et al. 2011, *The Astronomer's Telegram*, 3841, 1
- Renzo, M., Cantiello, M., Metzger, B. D., & Jiang, Y. F. 2020, *ApJ*, 904, L13
- Sablahit, G. N., Vink, J. S., Higgins, E. R., & Sander, A. A. C. 2022, *MNRAS*, 514, 3736
- Sablahit, G. N., Vink, J. S., Sander, A. A. C., & Higgins, E. R. 2023, *MNRAS*, 524, 1529
- Sander, A. A. C., Hamann, W. R., Todt, H., et al. 2019, *A&A*, 621, A92
- Sander, A. A. C. & Vink, J. S. 2020, *MNRAS*, 499, 873
- Santoliquido, F., Mapelli, M., Artale, M. C., & Boco, L. 2022, *MNRAS*, 516, 3297
- Santoliquido, F., Mapelli, M., Bouffanais, Y., et al. 2020, *ApJ*, 898, 152
- Santoliquido, F., Mapelli, M., Giacobbo, N., Bouffanais, Y., & Artale, M. C. 2021, *MNRAS*, 502, 4877
- Santoliquido, F., Mapelli, M., Iorio, G., et al. 2023, *MNRAS*, 524, 307
- Sawicki, M., Arnouts, S., Huang, J., et al. 2019, *MNRAS*, 489, 5202
- Schaye, J., Crain, R. A., Bower, R. G., et al. 2015, *MNRAS*, 446, 521
- Schulze, S., Fransson, C., Kozyreva, A., et al. 2024, *A&A*, 683, A223
- Schwarzschild, M. 1958, *Structure and evolution of the stars*.
- Sgalletta, C., Mapelli, M., Boco, L., et al. 2024, arXiv e-prints, arXiv:2410.21401
- Song, H., Meynet, G., Li, Z., et al. 2020, *ApJ*, 892, 41
- Spera, M. & Mapelli, M. 2017, *MNRAS*, 470, 4739
- Spera, M., Mapelli, M., Giacobbo, N., et al. 2019, *MNRAS*, 485, 889
- Springel, V., White, S. D. M., Jenkins, A., et al. 2005, *Nature*, 435, 629
- Takahashi, K. 2018, *ApJ*, 863, 153
- Tanikawa, A., Moriya, T. J., Tominaga, N., & Yoshida, N. 2023, *MNRAS*, 519, L32
- Tanikawa, A., Susa, H., Yoshida, T., Trani, A. A., & Kinugawa, T. 2021, *ApJ*, 910, 30
- The pandas development Team. 2024, *pandas-dev/pandas: Pandas*
- Vink, J. S. 2023, *A&A*, 679, L9
- Vink, J. S., de Koter, A., & Lamers, H. J. G. L. M. 2000, *A&A*, 362, 295
- Vink, J. S., de Koter, A., & Lamers, H. J. G. L. M. 2001, *A&A*, 369, 574
- Vink, J. S. & Gräfener, G. 2012, *ApJ*, 751, L34
- Vink, J. S., Higgins, E. R., Sander, A. A. C., & Sablahit, G. N. 2021, *MNRAS*, 504, 146
- Vink, J. S., Muijres, L. E., Anthonisse, B., et al. 2011, *A&A*, 531, A132
- Virtanen, P., Gommers, R., Oliphant, T. E., et al. 2020, *Nature Methods*, 17, 261
- Winch, E. R. J., Sablahit, G. N., Vink, J. S., & Higgins, E. R. 2025, arXiv e-prints, arXiv:2504.17009
- Woosley, S. E. 2017, *ApJ*, 836, 244
- Woosley, S. E., Blinnikov, S., & Heger, A. 2007, *Nature*, 450, 390
- Woosley, S. E. & Heger, A. 2021, *ApJ*, 912, L31
- Woosley, S. E., Heger, A., & Weaver, T. A. 2002, *Reviews of Modern Physics*, 74, 1015
- Yokoyama, T. & Tominaga, N. 2012, in *Astronomical Society of the Pacific Conference Series*, Vol. 458, *Galactic Archaeology: Near-Field Cosmology and the Formation of the Milky Way*, ed. W. Aoki, M. Ishigaki, T. Suda, T. Tsujimoto, & N. Arimoto, 51
- Yoshida, T., Umeda, H., Maeda, K., & Ishii, T. 2016, *MNRAS*, 457, 351
- Yungelson, L. R., van den Heuvel, E. P. J., Vink, J. S., Portegies Zwart, S. F., & de Koter, A. 2008, *A&A*, 477, 223
- Yusof, N., Hirschi, R., Meynet, G., et al. 2013, *MNRAS*, 433, 1114

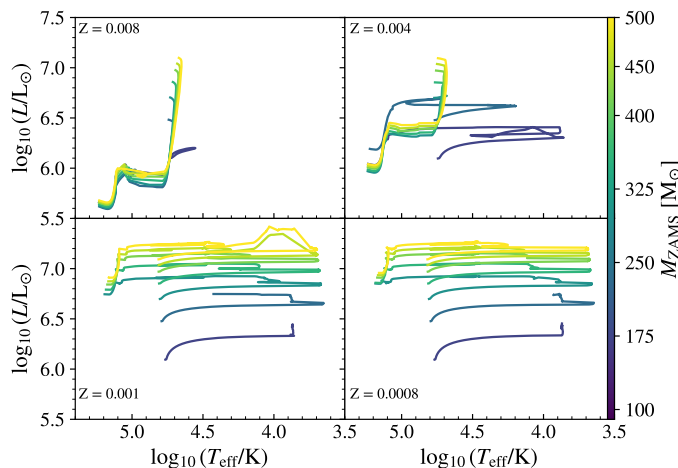


Fig. A.1: HR diagram of the simulated models. We report four selected metallicities: $Z = 0.008$, 0.004 , 0.001 , and 0.0008 .

Appendix A: MESA models

Here, we summarize the main properties of our MESA models, including the evolution of luminosity (L) and effective temperature (T_{eff}) in the Hertzsprung-Russell (HR) diagram (Fig. A.1), the radius (Fig. A.2) and the He core mass (Fig. A.3) until the end of core-He burning.

Figure A.1 shows the tracks in the HR diagram. All the models at low metallicity ($Z \leq 0.001$) do not develop optically thick winds during the main sequence. These models evolve horizontally in the HR diagram towards cooler temperatures and the mass loss is not high enough to cause a drop in luminosity. Certain models at higher metallicity, e.g. the $M_{\text{ZAMS}} = 100 M_{\odot}$ model at $Z = 0.008$, go back to the blue part of the HR diagram after entering the high- Γ_{Edd} phase. At these metallicities, the more massive stars enter the high- Γ_{Edd} regime just after the ZAMS, delineating the boundary between two distinct evolutionary behaviors: these stars evolve vertically in the HR diagram, exhibiting a steep decline in luminosity while remaining within a narrow range of temperature.

The radii of stars that enter the enhanced wind regime immediately after the ZAMS rapidly decrease as a consequence of the large amount of mass loss: indeed, in these cases, the H-rich envelope is quickly lost and also mass from the inner regions of the star is expelled (Fig. A.2). In the models that switch to high- Γ_{Edd} regime during the main-sequence, the radius reaches the peak at ~ 2 Myr and then decreases. When the models enter this regime in the very last part of the main sequence, the mass loss is not able to contrast the inflation and the radius grows up to $\log(R/R_{\odot}) \sim 3.5$ in a short timescale. In all the models, the radii decrease rapidly after the ignition of the He core.

Figure A.3 shows the evolution of the He-core mass, while Table A.1 reports the final values of the He core mass, at the end of core-He burning. At $Z = 0.008$, the mass of the He core decreases quickly because of wind mass loss, and all models end their life with $13.7 M_{\odot} \leq M_{\text{He,f}} \leq 20 M_{\odot}$. These systems cannot enter the pair-instability regime and undergo a core-collapse supernova. Lowering the metallicity, at $Z = 0.004$, only stars with $150 M_{\odot} \leq M_{\text{ZAMS}} \leq 200 M_{\odot}$ can experience PPISNe, while in all the other cases we find $M_{\text{He,f}} < 32 M_{\odot}$. At $Z = 0.001$, stars can experience different fates: only the $M_{\text{ZAMS}} = 50 M_{\odot}$ model undergoes a core-collapse supernova;

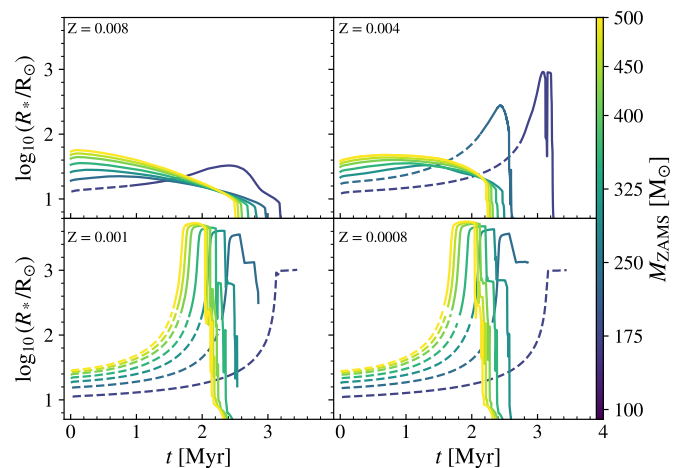


Fig. A.2: Time evolution of the radius. We report four selected metallicities: $Z = 0.008$, 0.004 , 0.001 , and 0.0008 . The solid lines show the evolutionary phase in which the stars enter the optically thick regime ($\Gamma_{\text{Edd}} > \Gamma_{\text{Edd,tr}}$), while the dashed lines represent the optically thin phase of stellar winds.

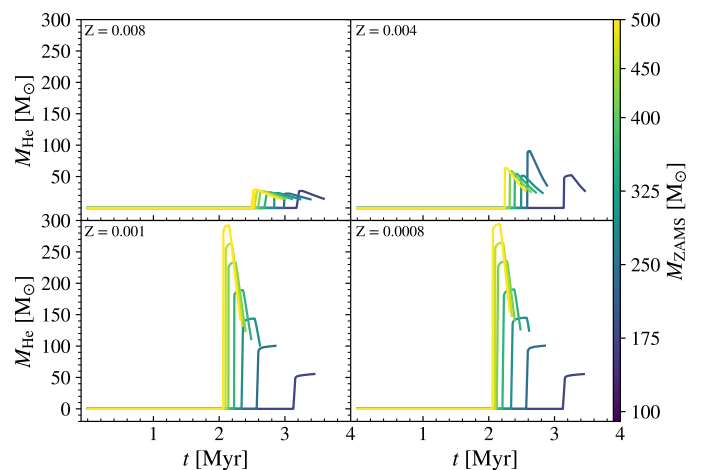


Fig. A.3: He core mass evolution as a function of time. From top-left to bottom-right: $Z = 0.008$, 0.004 , 0.001 , and 0.0008 .

models with $M_{\text{ZAMS}} = 75, 100 M_{\odot}$ go through PPISN, while models with $125 M_{\odot} \leq M_{\text{ZAMS}} \leq 450 M_{\odot}$ can experience PISNe. Finally, if $M_{\text{ZAMS}} = 475, 500 M_{\odot}$ the model directly collapses onto a black hole. At even lower metallicity ($Z = 0.0008$), the initial stellar mass range of systems that can undergo a PISN is reduced: $125 M_{\odot} \leq M_{\text{ZAMS}} \leq 350 M_{\odot}$.

Appendix B: PARSEC models

Our comparison sample is based on PARSEC stellar tracks, which have been extensively discussed by Costa et al. (2025); see also Bressan et al. (2012); Chen et al. (2015); Costa et al. (2022); Nguyen et al. (2022); Iorio et al. (2023); Costa et al. (2023) for additional references. Here, we briefly summarize their main properties.

$M_{ZAMS} [M_{\odot}]$	Final He core mass [M_{\odot}]			
	$Z = 0.008$	$Z = 0.004$	$Z = 0.001$	$Z = 0.0008$
50	19.9	25.3	24.7	24.7
75	17.7	32.4	39.9	40.1
100	14.7	27.2	55.5	55.4
125	13.8	28.9	70.6	70.6
150	13.7	32.2	85.6	85.6
175	13.7	35.7	100.5	100.7
200	13.8	39.4	109.7	115.6
225	13.8	23.8	105.4	129.2
250	13.9	23.9	101.1	124.5
275	13.9	24.1	104.6	124.1
300	14.1	24.4	107.3	127.2
325	14.2	24.6	111.3	126.6
350	14.3	24.9	116.1	131.7
375	14.4	25.2	118.7	132.9
400	14.5	25.5	123.8	140.9
425	14.7	25.9	127.7	142.2
450	14.8	26.2	132.2	148.1
475	14.9	26.6	135.8	151.6
500	15.1	27.1	142.1	155.5

Table A.1: Final mass of the He core of the single stellar model at $Z = 0.008$ (second column), $Z = 0.004$ (third column), $Z = 0.001$ (fourth column) $Z = 0.0008$ (fifth column). In the first column is reported the initial total mass of the corresponding star.

For the winds of massive O-type stars, PARSEC adopts the fitting formulas by [Vink et al. \(2000\)](#) and [Vink et al. \(2001\)](#), with a correction introduced by [Chen et al. \(2015\)](#) to account for the effects of electron scattering, based on the models of [Gräfener & Hamann \(2008\)](#). In this framework, the mass-loss rate of an O-type star scales as $\dot{M} \propto Z^{\beta}$, where Z is the metallicity and the exponent β depends on the Eddington ratio Γ_{Edd} : $\beta = 0.85$ for $\Gamma_{\text{Edd}} < 2/3$, $\beta = 2.45 - 2.4 \times \Gamma_{\text{Edd}}$ for $2/3 \leq \Gamma_{\text{Edd}} < 1$, and $\beta = 0.05$ for $\Gamma_{\text{Edd}} \geq 1$ ([Chen et al. 2015](#)). This formalism provides a fit to the models by [Gräfener & Hamann \(2008\)](#) and [Vink et al. \(2011\)](#), incorporating the dependence of mass loss on the Eddington ratio.

For Wolf–Rayet (WR) stars, PARSEC adopts the prescriptions by [Sander et al. \(2019\)](#), which successfully reproduce the observed properties of Galactic WR stars of type C (WC) and type O (WO).

PARSEC models include internal mixing by adopting the mixing-length theory (MLT; [Böhm-Vitense 1958](#)), calibrated on the Sun with a mixing-length parameter $\alpha_{\text{MLT}} = 1.74$ ([Bressan et al. 2012](#)). Convective regions are identified using the Schwarzschild criterion ([Schwarzschild 1958](#)), as implemented in [Bressan et al. \(1981\)](#). The PARSEC tracks used in this work assume an overshooting parameter of $\lambda_{\text{ov}} = 0.5$, where λ_{ov} represents the mean free path of convective elements beyond the convective boundary, expressed in units of the pressure scale height. In addition, an envelope undershooting distance of $\Lambda_{\text{env}} = 0.7$ pressure scale heights is adopted.